

Antenna Aperture Localization for Arrival Time Correction Using First-Break

Kay Y. Liu*, Elise C. Fear, and Mike E. Potter

Abstract—For microwave imaging systems that utilize antennas with spatially separated feeds and apertures, arrival time correction based on the antenna aperture location is one of the fundamental steps in radar data processing. The estimates of the antenna aperture time and the corresponding average velocity in the material in contact with the antenna are expected to have a significant impact on the quality of the reconstructed image. In this paper, we propose antenna aperture and average velocity estimation by least-squares regression analysis of the first-breaks. The results indicate that the proposed method is able to process either the reflection data or the transmission data measured by antennas with different structures. Compared to those readily identifiable characteristics in the signal, the first-break is less influenced by waveform distortion and is able to provide more consistent reference. Differences in the images of test objects are also noted.

1. INTRODUCTION

The last decade has seen growing investigation of medical imaging techniques with low-power, microwave-frequency electromagnetic (EM) waves. In particular, microwave detection of breast tumors is a potential nonionizing alternative being investigated by a number of groups [1–5]. In these microwave-based systems, in a similar fashion to ground penetrating radars, microwaves are transmitted from an antenna or antenna array, and the received signals, which contain reflections from targets, are recorded and analyzed.

Some of these deployed antennas have a feed and an aperture that are not spatially co-located [2–5]. For antennas where this distance is significant with respect to wavelengths of interest, this spatial difference gives rise to the need for determining the wave propagation time between the antenna feed and the aperture. The antenna aperture serves as a reference imaging location in the signal, so identifying this aperture is one of the fundamental steps in microwave imaging. Additionally, a variety of immersion liquids have been commonly used in microwave imaging systems for the purpose of effectively coupling the microwave signal into the object, and/or attenuating unwanted reflections [6]. The average velocity that the wavelet propagates in the immersion liquid needs to be estimated in order to determine the travel time between the antenna aperture and the object. Both the antenna aperture time and the average velocity in the material in contact with antenna have significant impact on the accuracy of response time and average velocity when the wave propagates through the imaged object, which ultimately affect the quality of the reconstructed image.

At the University of Calgary, we are developing an approach to microwave breast imaging termed tissue sensing adaptive radar (TSAR) [4]. The antenna aperture and the corresponding average velocity of the immersion liquid are estimated based on the readily identifiable characteristics, such as the peak response or a zero-crossing, in a pair of signals that are recorded by placing a reflector at two different locations. This may yield a reasonable result in the idealistic case that excludes waveform

Received 19 December 2014, Accepted 5 February 2015, Scheduled 16 February 2015

* Corresponding author: Kay Yuhong Liu (yuliu@ucalgary.ca).

The authors are with the Department of Electrical and Computer Engineering, University of Calgary, 2500 University Dr. NW, Calgary, AB T2N 1N4, Canada.

modification from noise, nonstationarity of wave propagation in dispersive media, and/or superposition of multiple wavelets. However, in practice, any of these factors are unavoidable. Given the waveform distortion, these readily identifiable waveform features are likely to be influenced and cannot be used as consistent references to provide reliable estimates. Moreover, since only two samples are involved for the estimation, the solution can be easily influenced by the error included in the dataset.

In this paper, we propose our approach to antenna aperture and average velocity estimation via a least-squares regression analysis of the first-breaks. In wave propagation, the first-break is defined as the first wave from a discrete source impulse, naturally or artificially generated, that is recorded at a detector [7]. Compared to those readily identifiable characteristics in the signals, the advantage of using the first-break time is that it is less influenced by waveform modification. In seismic imaging, the first-breaks associated with the refracted arrival times are commonly used in an inversion scheme to study the near-surface low-velocity zone and in the subsequent determination of static corrections [8]. In this study, we adapt these ideas from seismic imaging to microwave imaging and demonstrate that (1) the first-break method can work with either the reflection or the transmission data that are measured by antennas with different designs; and (2) the first-breaks are able to provide consistent estimation of the antenna aperture and the corresponding average velocity in the presence of waveform distortion due to the dissipation and dispersion of wave propagation, the superposition of multiple pulses, and different excitation pulses.

The rest of this paper is organized as follows. In Section 2, the proposed approaches are described in detail. Section 3 presents a description of the conducted simulations and experiments, the data processing flow, and a set of metrics for result assessment. In Section 4, the results obtained from simulated and experimental data are presented to demonstrate the consistency and accuracy of first-break estimates in the presence of various waveform modifications. Section 5 concludes the paper.

2. METHODOLOGY

The section starts with a description of the selected first-break picking algorithm. Then, the approach to estimate antenna aperture and the corresponding average velocity via the least-squares regression analysis of the first-breaks is presented. Finally, an iterative correction procedure is provided for optimizing the first-break picks and improving the estimation accuracy of the least-squares fit.

2.1. First-Break Picking Based on Modified Energy Ratio Attribute

Picking the first-break time is the task of determining the onsets of the first signal arrivals as accurately as possible. The first-break quality is related to the near-surface structure, source type, and signal-to-noise ratio (SNR) [9]. Among numerous techniques developed for detecting first-breaks automatically or semi-automatically [9–15], we choose the scheme for individual time series based on a modified energy ratio (MER) attribute [10, 15] because it is very robust when SNR is sufficiently high and able to provide consistent and reliable picks when the pulse shape varies. The MER algorithm is described as below.

Assume a time series $s(i)$, in which the time index $i = 1, 2, \dots, N$. For any given time sample $s(i)$, two energy windows can be constructed on each side of $s(i)$. Let the number of points in each energy window be N_e , which is normally chosen as three times of the distance between two adjacent peak values in the signal. The energy ratio (ER) between those two windows is calculated as

$$er = \frac{\sum_{j=i}^{i+N_e} s^2(j)}{\sum_{j=i-N_e}^i s^2(j)}, \quad (1)$$

in which, if $j \leq 0$, $s(j) = (s(1) + s(2))/2$; otherwise, if $j > N$, $s(j) = (s(N-1) + s(N))/2$.

Given (1), the modified energy ratio at sample $s(i)$, denoted as $mer(i)$, can be calculated as

$$mer(i) = (|s(i)| \times er)^3. \quad (2)$$

The first break of the time series $s(i)$ is indicated by the $mer(i)$ that gives the largest amplitude. An example is provided in Figure 1 to illustrate how the above procedure works. In Figure 1(a), the energy windows are the two regions on each side of the sample delimited by the dash lines. The modified energy ratio for each sample is shown in Figure 1(b). The sample corresponding to the largest ER is picked as the first-break in the given signal.

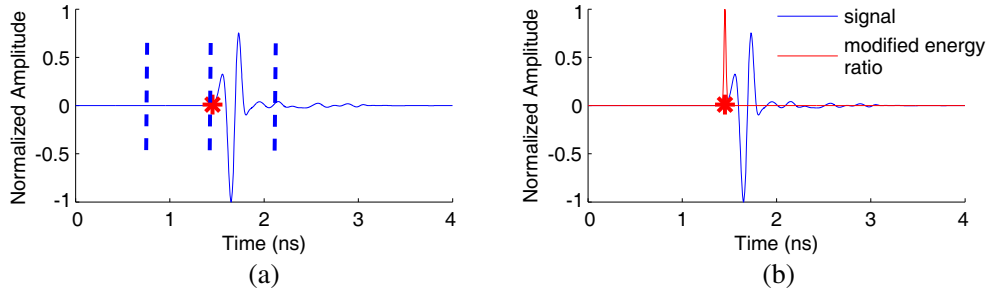


Figure 1. Demonstration of first-break picking with the MER algorithm. (a) Definition of energy windows. (b) First-break determination based on the largest energy ratio. Normalized amplitude is plotted for presentation purpose. The sample in the signal is represented by the red ‘*’.

2.2. First-break Estimation of Antenna Aperture and Average Velocity

Using the first-break as reference feature, the following describes the approach of least-squares regression analysis for estimating the antenna aperture time and the corresponding average velocity in the material in contact with the antenna.

In Figure 2, the signals are simulated reflections from a perfect electric conducting plate (PEC) placed at a range of distances from the balanced antipodal Vivaldi antenna with a director (BAVA-D) [16]. For convenience, we assume that the antenna aperture lies at the origin (0, 0), which is Δx away from the excitation point, i.e., time 0. The goal here is to figure out Δt , i.e., the two-way time delay of the antenna aperture response relative to the excitation point. With this in mind, the reflections from the PEC positioned at a number of locations are collected, denoted as P_k , $k = 1, \dots, M$. For the k th reflection, t_k is the first-break time determined by the MER technique and x_k is the distance between the k th plate and the antenna aperture. As shown in Figure 2, a straight line can be fit to the collection of points. The line intercept and slope are calculated by Pearsons coefficient of correlation [17]. The inverse of the line slope gives the average velocity (v) of wave travel in the background medium. Thus, by extrapolating this line from any PEC location back to antenna aperture, i.e., $x = 0$, we have

$$t_k = 2x_k/v + \Delta t. \tag{3}$$

Therefore, the antenna aperture location in time can be determined as

$$\Delta t = t_k - 2x_k/v. \tag{4}$$

Using PEC reflections as an example, the above describes the basic principle of least-squares regression analysis of the first-breaks for antenna aperture and average velocity estimation. This

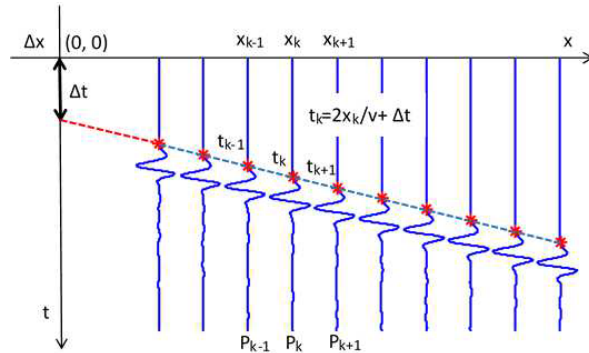


Figure 2. Schematic diagram of antenna aperture localization using the first-break picks. The red ‘*’ represents the first-break on each PEC or metal plate reflection. The red dash line represents the extrapolation from any known PEC or metal plate location to antenna aperture. The blue dash line represents the line approximated from the first-break picks.

approach can also be applied to sets of signals that are recorded when placing a calibration object at various distances away from the antenna aperture.

2.3. First-Break Correction for Optimizing Linear Regression Model

The MER algorithm searches for the first-break in a single signal, however errors may be reduced by including knowledge of the first-breaks in multiple signals using constraints. With this in mind, we developed a mis-pick correcting procedure to restrict the search of the first-breaks to the proximity of the straight line, which is obtained by applying least-squares regression analysis to the signal-by-signal picks. As a result, mis-picks can be corrected or discarded using simple criteria.

The mis-pick correction is implemented via an iterative process. The first step consists of a signal-by-signal first-break picking using the MER algorithm. A straight line is constructed via the least-squares regression analysis of these first-breaks; then, the distance (error) between each pick and the least-squares fit is calculated. If the error is larger than 3ζ (where ζ is the standard deviation of the fit), the pick is either rejected or adjusted. Methods of adjustment typically involve user selection and may include identifying the second or third largest ER values based on the common-sense factors, such as constant time delay between adjacent signals, time increase with distance, first-break alignment along straight lines, etc.. With the updated set of picks, the straight line is recalculated accordingly. This process is repeated until there are no picks with errors greater than 3ζ . The final result of this iterative process is a set of properly picked first-breaks in signals.

3. DATA ACQUISITION AND PROCESSING

In this section, we describe the simulations and experiments that are conducted to test the consistency and accuracy of antenna aperture and average velocity estimated by the proposed first-break technique. The data are collected with two ultra-wideband (UWB) sensors developed for near-field microwave imaging and sensing, namely the BAVA-D [16] and Nahanni [18] antennas. The BAVA-D sensor is able to produce a narrow beamwidth and generally high fidelity while keeping S_{11} below -10 dB between 2.4 to 18 GHz. The BAVA-D antenna is designed to operate when immersed in canola oil. The Nahanni sensor is able to transmit and receive electromagnetic energy from 1.8 to 12 GHz, and produce stable radiation patterns over this range. The Nahanni is shielded and does not require an immersion liquid. In this paper, unless specified, the antenna behaves as both transmitter and receiver, i.e., monostatic radar.

All simulations are performed using SEMCAD X (SPEAG, Zürich, Switzerland), which utilizes the finite-difference-time-domain (FDTD) technique. For all the simulations included in this paper, the perfectly matched layers (PML) boundary condition is applied in order to avoid reflections from the boundary of simulation space. A tool in FDTD simulations is used to convert signals recorded at port to S -parameters. As data are recorded in the frequency domain, for both simulated and measured data, different waveforms are used to weight the data in order to demonstrate the robustness of the first-break method to a variety of excitation pulses. The current TSAR processing flow [4] is utilized for data analysis and image reconstruction.

3.1. PEC Simulations

The PEC simulations are conducted with both BAVA-D and Nahanni antennas. Figure 3 illustrates the simulation setup.

With the BAVA-D antenna, the reflected signals are collected to estimate the antenna aperture and the corresponding average velocity in low loss and non-dispersive immersion medium. The BAVA-D antenna uses canola oil as an ambient immersion medium, which is usually considered as non-dispersive. From 1 to 14 GHz, its permittivity varies from 2.55 to 2.35 and conductivity varies from 0.01 S/m to 0.04 S/m. Therefore, it is sufficient to describe this immersion medium using an average relative permittivity value of $\epsilon_r = 2.5$ and the maximum conductivity of $\sigma = 0.04$ S/m. The BAVA-D simulation is shown in Figure 3(a). Unless specified, this layout is used for all the PEC simulations or the metal plate measurements demonstrated in this paper.

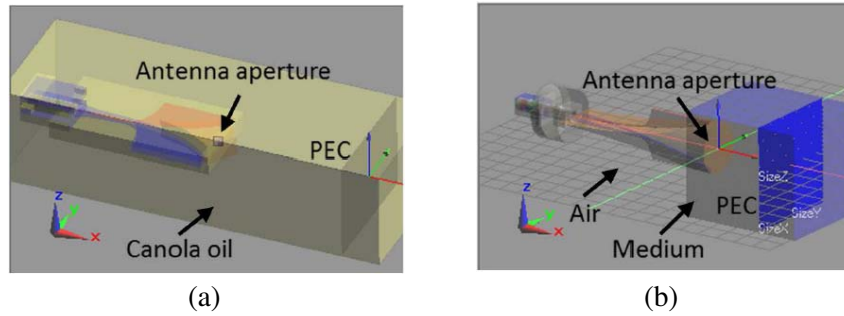


Figure 3. Setup of PEC simulation with (a) BAVA-D antenna and (b) Nahanni antenna. The PEC plate is parallel to the yz plane and perpendicular to the x axis. The center of antenna radiation is along the $+x$ direction. Ten PEC reflections are simulated by shifting the PEC plate from 10 mm to 100 mm away from the antenna aperture.

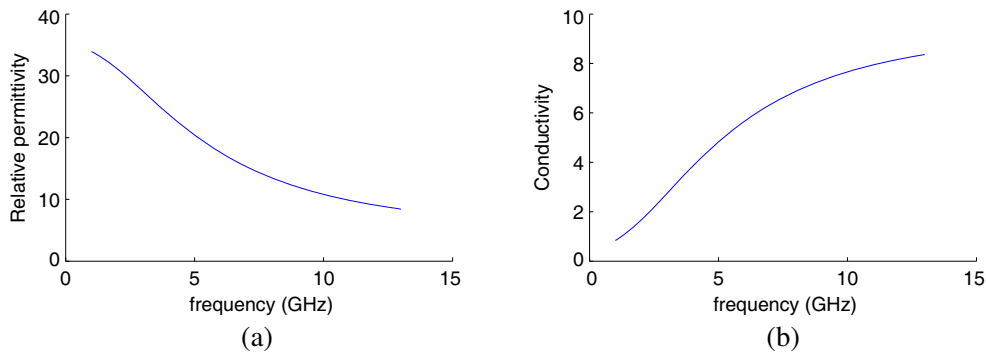


Figure 4. The dielectric properties of lossy dispersive immersion medium. The frequency dependent behavior is described with a single pole Debye model having parameters of static conductivity $\sigma = 0.52$ S/m, relative permittivity at the infinite frequency $\epsilon_{\infty} = 4.0$, relative static permittivity $\epsilon_s = 35.0$, and relaxation time $\tau = 30.0$ ps.

With the Nahanni antenna, the PEC reflections are acquired with both non-dispersive and dispersive immersion media to investigate the consistency of the first-break time in the presence of waveform modification due to dissipation and dispersion. While canola oil is used as non-dispersive immersion medium, the behavior of the dispersive immersion medium is shown in Figure 4. As shown in Figure 3(b), the Nahanni simulations share the same setup as the BAVA-D simulations in terms of the direction of antenna radiation center, the orientation of PEC plates, and the distance variation between the PEC plate and the antenna aperture, except that the background is divided into two regions. The region enclosing the antenna has the dielectric properties of free space, and the region that the antenna radiates into has the dielectric properties of either canola oil or the lossy dispersive material.

3.2. Dielectric Sphere Simulations

The sphere simulations are conducted with the BAVA-D antenna to generate data that include waveform modification due to the superposition of multiple pulses. The setup of the simulation is displayed in Figure 5. The homogeneous sphere is lossy or lossless with a relative permittivity value of $\epsilon_r = 10$. The sphere diameters vary from 2 mm to 20 mm with increment of 2 mm. The distance between the sphere center and the antenna aperture is 80 mm. 2D data acquisition is performed by rotating the antenna around the center of sphere and collecting the responses from 40 different locations.

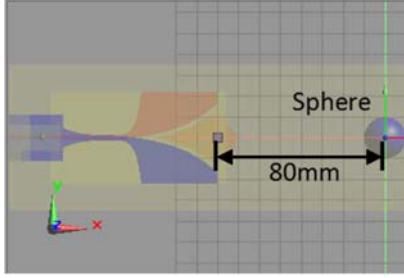


Figure 5. Setup of sphere simulation with BAVA-D antenna.

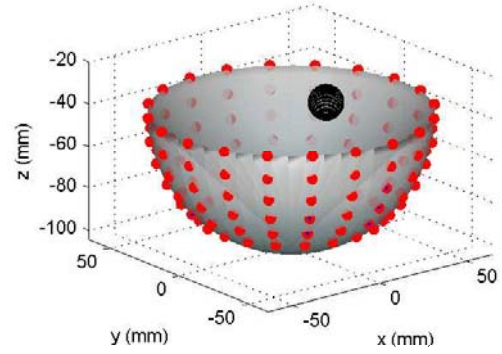


Figure 6. The antenna position relative to the tumor phantom. The red dots represent the antennas, and the black sphere represents the tumor.

3.3. Tumor Phantom Reflection Measurements

Reflection measurements are collected using the TSAR breast imaging system [4], which incorporates the BAVA-D antenna. The measurements are obtained with an 8719ES Vector Network Analyzer (VNA) (Agilent, Palo Alto, CA). As shown in Figure 6, the antenna is repositioned to a total of 120 locations over a pre-calculated hemispherical surface. At each scan location, the position of the antenna is normal to the hemispherical surface. In the results presented in this paper, reflection data are measured from a carbon-based tumor phantom [19]. The tumor is roughly spherical and centered at $(20 \text{ mm}, 0, -40 \text{ mm})$ with a diameter of 16 mm. The Debye parameters of the carbon-based material are static conductivity $\sigma = 5.035 \text{ S/m}$, relative permittivity at the infinite frequency $\epsilon_{\infty} = 23.28$, relative static permittivity $\epsilon_s = 84.11$, and relaxation time $\tau = 60.95 \text{ ps}$.

3.4. Dielectric Slab Transmission Measurements

The transmission measurements are collected using the Nahanni transmission measurement system [20], shown in Figure 7. The hardware consists of Nahanni antennas assembled into two arrays containing five elements each. The lower array (shown in Figure 7(b)) is fixed while the upper one (shown in Figure 7(a)) can translate to come into contact with the measured object. Both arrays have an electromechanical switch permitting the selection of one sensor at a time. For each pair of selected sensors, a full matrix of S parameters are measured with a VNA (PNA-X, Agilent, Palo Alto, CA). In this paper, the transmission measurements are collected from a homogeneous dielectric slab (Eccostock HiK, Emerson and Cuming Microwave Products) having a relative permittivity value of $\epsilon_r = 15$ and thickness of 25.4 mm.

The following steps are taken in order to determine the wave travel time between the transmitting and receiving antennas. First of all, for each antenna, the first-break is picked using the MER algorithm in the S_{ii} signal that has been calibrated by removing the antenna only response. By antenna only response, we mean the S_{ii} signal that is recorded without the presence of an object. Since the aperture of Nahanni antenna directly contacts with the dielectric slab, the first-break time is the same as the time that it takes the signal to propagate from the feed to aperture (termed aperture time). Secondly, the first-break in the S_{ij} signal is picked. This first-break time needs to be corrected by removing the aperture time of both the transmitting and receiving antennas in order to obtain the wave travel time between each pair of antennas. Given the acquisition geometry and the wave travel time, the average velocity of wave propagation in the dielectric slab can be estimated by following the approach described in Section 2.2.



Figure 7. Setup of Nahanni transmission measurement system. (a) View of the upper array consisting of five Nahanni sensors, and (b) view of the lower array consisting of five Nahanni sensors. In (a) and (b), the brown circle on the upper and the lower arrays indicates the aperture of Nahanni sensor.

3.5. Data Processing

The following steps are taken to process the reflection-based data and reconstruct the images.

- (i) *Remove the antenna response from recorded data.* Two sets of data are recorded, one with and one without the presence of an object. The reflection coefficients (S_{ii}) are calibrated by subtracting the antenna only response from the data recorded with the presence of object.
- (ii) *Convert S -parameters to time signals.* The time signal is created from the frequency domain S -parameters. Given a pulse specified in time domain, a chirp-z transform [21] is used to find its frequency representation at the measured frequencies. The measured S -parameters are weighted with the frequency spectrum of the given pulse. Finally, the inverse chirp-z transform [21] is used to convert the weighted S -parameters from frequency domain to time domain. In this paper, unless specified, the measured S -parameters are weighted by a differentiated Gaussian pulse.
- (iii) *Correct time zero to the antenna aperture location.* Estimate the antenna aperture location in the signal by following the approach described in Section 2.2. Clip off the signal prior to the estimated antenna aperture.
- (iv) *Reconstruct images.* Image reconstruction is performed using the confocal imaging approach described in [4].

3.6. Metrics

The following metrics are utilized in order to quantitatively assess the quality of reconstructed images given the antenna aperture location. These metrics are applicable to point objects rather than larger objects.

Inclusion location error is defined as the distance between the actual location and the maximal inclusion response on the image.

The FWHM assesses the physical extent of the inclusion on the image. It is defined as the distance from the maximal inclusion response to where the backscattered energy drops by half. It is computed through the center of the inclusion location in the x -, y -, and z -directions.

The SMR is given as

$$\text{SMR} = 10 \log (E_{\text{Inclusion}}/E_{\text{Reference}}), \quad (5)$$

where $E_{\text{Inclusion}}$ is the average energy computed over the inclusion region and $E_{\text{Reference}}$ the average energy over a reference region. The inclusion region is centered at the voxel with maximum magnitude after focusing, and has the dimension of n_x by n_y by n_z voxels. Here, n_x , n_y , and n_z are determined by the physical size of the inclusion. The reference region can be either the entire imaging grid or a second selected region outside the inclusion area.

4. RESULTS AND DISCUSSION

Using BAVA-D and Nahanni antennas, we test the performance of the first-break method with simulated and measured data. The results are presented in this section to demonstrate the consistency and accuracy of the first-break method in the case of waveform modification due to lossy dispersive propagation media, the superposition of multiple pulses, and the variation of excitation pulses.

4.1. Waveform Modification Due to Dispersive Media

With canola oil as the immersion liquid, Figure 8 shows the results obtained from the simulated PEC reflections that are recorded by the Nahanni antenna. In Figure 8(a), from top to bottom, the PEC plate is placed 20 mm to 100 mm from the antenna aperture. It can be seen that the waveform is well preserved when the wave propagates in low loss and non-dispersive canola oil. Points on the signal indicate first-break and peak detection results. In this case, ‘peak’ means the maximum absolute amplitude. Figure 8(b) plots the location versus the time of arrival of these points, along with the least-squares best-fit lines. The inverse of the slope of these lines is used to estimate velocities of 1.92×10^8 m/s (first-break) and 1.97×10^8 m/s (peak). The first-break estimate has a smaller error compared to the analytical calculation of 1.90×10^8 m/s for canola oil. In Figure 8(b), an apparent difference is observed in the aperture time estimated by two different approaches. This is because, using the first-break as references, the antenna aperture is estimated in terms of the initial time of onset; using the peak as references, the antenna aperture is estimated in terms of the time that the signal achieves its maximum negative value.

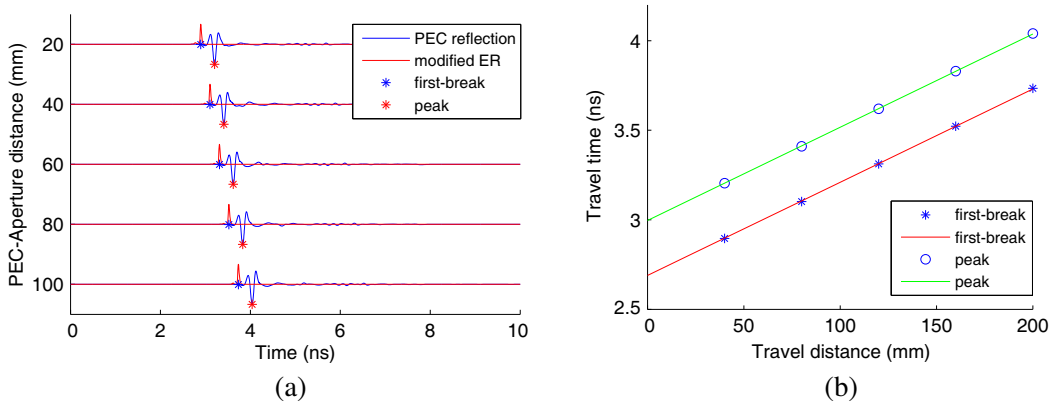


Figure 8. (a) Nahanni measurements of PEC reflection in canola oil. The vertical axis indicates the distance between the PEC and the antenna aperture. Normalized amplitude is plotted for the PEC reflection and the modified ER. (b) Antenna aperture and average velocity estimation with the first-break time and the peak time.

The results obtained from wave propagation through the dispersive medium are shown in Figure 9. Due to the frequency-dependent dispersion and attenuation, the waveform changes during propagation, which affects the identifiable characteristics, such as the first peak location, the zero-crossing, etc., in the signal. This modification in the waveform affects the peak location, but not the onset location. Therefore, a discrepancy is observed between the first-break estimates and the peak estimates as shown in Figure 9(b). The average velocities estimated with the first-break time and the peak time are 6.0×10^7 m/s and 4.67×10^7 m/s, respectively. To evaluate these results, we calculate the average velocity of the dispersive medium as follows. Given the Debye parameters in Section 3.1, a single pole Debye model [22] is utilized to calculate the complex relative permittivity. Then, the phase velocity over the excitation frequencies (i.e., between 1 GHz and 13 GHz) is calculated based on the complex relative permittivity and weighted by the amplitude spectrum of the excitation pulse. Finally, the average velocity is obtained by summing the weighted phase velocity over the excitation frequencies. With the differentiated Gaussian pulse, the average velocity is calculated as 6.09×10^7 m/s. This result

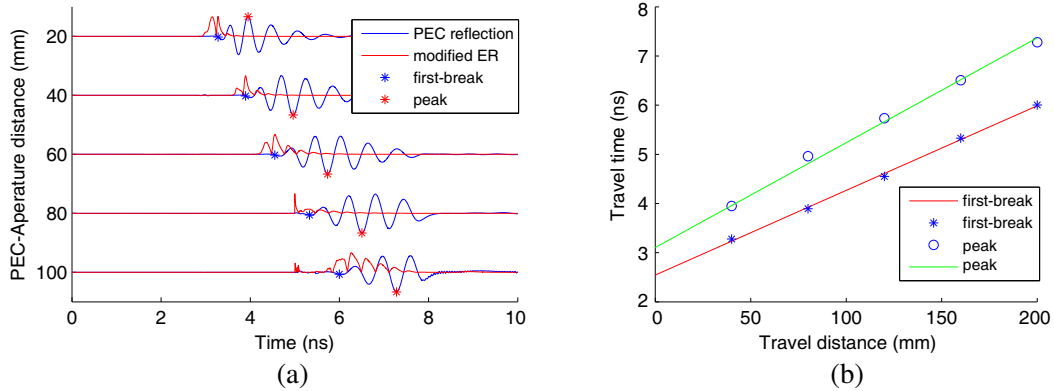


Figure 9. (a) Nahanni measurements of PEC reflection in lossy dispersive immersion medium. The vertical axis indicates the distance between the PEC and the antenna aperture. Normalized amplitude is plotted for the PEC reflection and the modified ER. (b) Antenna aperture and average velocity estimation with the first-break time and the peak time.

Table 1. Comparison of antenna aperture time and velocity estimated with different excitation pulses.

		Differentiated Gaussian Pulse	Gaussian Pulse
First-break	Antenna Aperture (ns)	2.59	2.66
	Velocity (m/s)	6.0×10^7	5.99×10^7
Peak	Antenna Aperture (ns)	3.10	3.00
	Velocity (m/s)	4.67×10^7	4.04×10^7

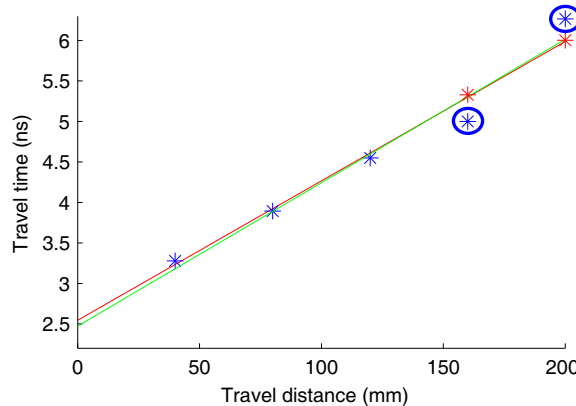


Figure 10. Demonstration of mis-pick correction. The blue ‘*’ represents the first-breaks before mis-pick correction and the green line is the least-squares fit of these picks. The red line is the best-fit line after correcting the mis-picks circled in blue to the right positions indicated by the red ‘*’.

indicates an error of 23.3% in the peak estimation, while 1.5% is the error in the first-break estimation. The underestimate of velocity with the peak time is due to the waveform gradually broadening with increasing travel distance, which leads to a delay in the selected peak time.

In the presence of dispersion, it is not immediately obvious which waveform feature provides the most representative measure of material properties or physical structure. In order to assess the consistency and accuracy of the estimates with the dispersive medium, a Gaussian pulse is applied as the excitation signal and the results are compared with those obtained with the differentiated Gaussian

pulse. Table 1 lists the antenna aperture and velocity estimated with different pulses. It can be seen that the first-break estimates of velocity are much more consistent than the peak estimates. The difference is less than 1% (0.27%) between the first-break estimated velocities; however, it is up to 16.45% between the velocities estimated by the peak time. On the other hand, consistent antenna aperture locations are obtained with both excitation pulses.

The mis-pick correction procedure is applied to the data set shown in Figure 9 in order to optimize the picked first-breaks. With the MER algorithm alone, the picks will be automatically determined at the sample location that shows the largest value of ER. However, based on our knowledge of the PEC spatial locations and the general rule of first-break alignment along straight lines, a judgment can be made that, in the signals acquired at the PEC locations of 80 mm and 100 mm away from the antenna aperture, the actual first-break should be picked from the sample location exhibiting the second or third largest ER values. The results are shown in Figure 10. In this case, there is no significant difference in the best-fit lines constructed before and after the mis-pick correction. This is because the incorrect picks are evenly distributed on each side of the best-fit line.

4.2. Waveform Modification Due to Superposition of Multiple Pulses

The overlapping of multiple pulses can also cause waveform modification in both dispersive and non-dispersive media. In microwave breast imaging, the tumor is often modeled as a spherical or cylindrical object. In [23], Ray et al. provide theoretical analyses on the response of a dielectric sphere for electromagnetic pulsed wave in near field. Their analyses indicate that the response waveforms of a dielectric sphere to the incident electromagnetic wave can be complicated by the multiple reflections and the multiple paths in the sphere. In this paper, our interest is to investigate how the modification of sphere response waveforms can affect the identifiable characteristics, such as the first peak and the zero-crossing, in the signal. Figure 11 displays the backscattering responses of spheres with diameters from 2 mm to 20 mm. Because the multiple reflections and multiple paths are affected by the size of sphere, modified response waveforms are observed from spheres with different diameters.

We estimate the antenna aperture and the wave travel velocity using the PEC reflections recorded by the BAVA-D antenna. Given these estimates, we calculate the onset time and the peak time in the sphere response based on the distance between the sphere surface and the antenna aperture. These values are shown with ‘*’ in Figure 11. We compare these calculated values to the MER picked onset time and the peak time based on the absolute maximum amplitude in the signal. These values are

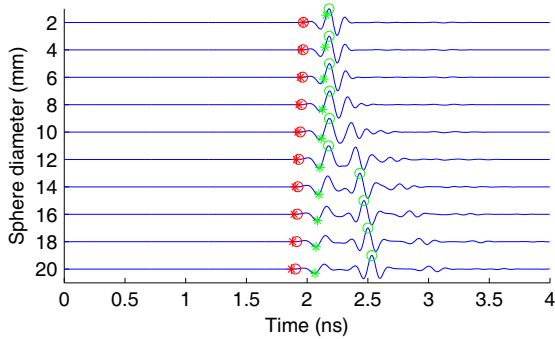


Figure 11. The response waveforms of lossless non-dispersive dielectric spheres placed in canola oil. The vertical axis indicates the sphere diameter. From top to bottom, the sphere diameters vary from 2 mm to 20 mm with increment 2 mm. Normalized amplitude is plotted for each sphere response. The onset time is represented by the red ‘*’ and ‘o’, and the peak time is represented by the green ‘*’ and ‘o’.

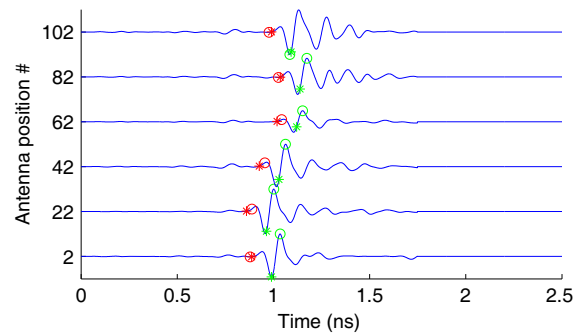


Figure 12. The response waveforms of lossy dispersive tumor phantom. The vertical axis indicates the antenna scan position. Normalized amplitude is plotted for the tumor response recorded at each antenna position. The onset time is represented by the red ‘*’ and ‘o’, and the peak time is represented by the green ‘*’ and ‘o’.

shown with ‘o’ in Figure 11. It can be seen that the calculated onset times match well with the MER picked ones. However, due to the waveform modification, there is a significant difference between the peak times that are calculated and identified on the signal. These results indicate that the first-break time is more consistent than other waveform features. Using the antenna aperture and average velocity estimated by the first-break picks, we can consistently derive the initial time of wave onset on the sphere surface.

4.3. Waveform Modification Due to Data Noise

While random noise may not cause significant modification in the original waveform, the presence of coherent noise can exaggerate the distortion of waveform. To assess the performance of the first-break method with real data contaminated by noise, the above procedure is applied to the tumor phantom responses recorded by the reflection measurement system described in Section 3.3. The results are shown in Figure 12 where the same denotations as those in Figure 11 are used. Among 120 signals, the six displayed signals are chosen from antennas at different vertical positions. The results indicate a good match between the calculated and the MER picked first-breaks with the tumor phantom measurements. There is a slight mismatch in the third and the fourth signals from top to bottom. This may be because, instead of a perfect sphere, the tumor phantom is roughly spherical; however, when calculating the distance between the antenna and the sphere, we assume a perfect spherical surface. On the other hand, due to the waveform modification, the calculated peak locations in general deviate from the true peak locations.

4.4. Waveform Modification in the Transmission Data

To test the performance of the first-break method with waveforms that include more severe distortion, the scattering responses of a homogeneous non-dispersive dielectric slab are recorded using the Nahanni transmission measurement system described in Section 3.4. Using one of the sensors in the lower array as transmitting sensor, the obtained results are shown in Figure 13. The top signal in Figure 13(a) is the back-scatter response of the dielectric slab recorded by the transmitting sensor, and the remaining five signals are the forward-scatter responses recorded by the receiving sensors in the upper antenna array. No pulse shaping is applied to the recorded signals in this case. It can be seen that the waveform of the reflected wave is significantly different from those of the transmitted waves. Between the transmitted waves, the waveforms are also different.

As shown in Figure 13(a), the first-break method is able to consistently pick up the onset time relative to the source pulse; however, the peak method fails to provide reliable peak location because

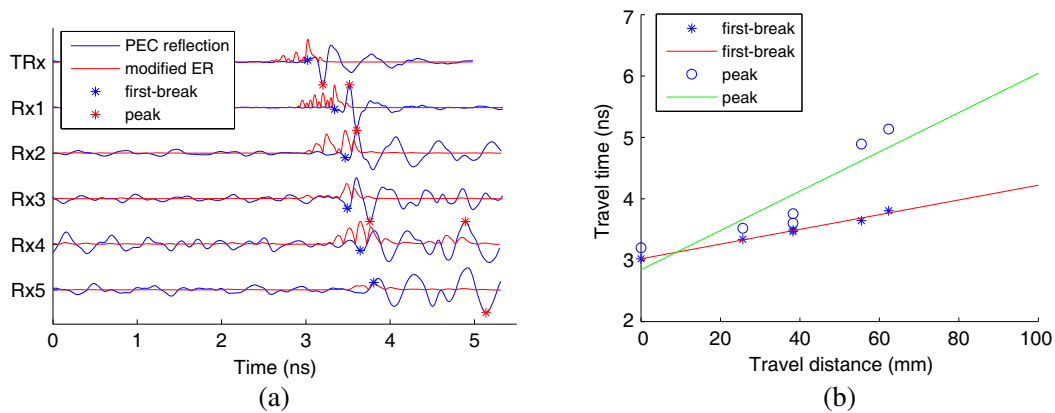


Figure 13. (a) Nahanni reflection and transmission measurements. In the vertical axis, ‘TRx’ indicates a reflection measurement and ‘Rx#’ indicates a transmission measurement. ‘#’ is to differentiate the receiving antennas. Normalized amplitude is plotted for each measured signal. (b) The least-squares best-fit lines constructed from the first-breaks and the peaks.

of the inconsistency in the waveform. Consequently, a great discrepancy is observed in the antenna aperture and velocity estimated using these onset times and peak times. In Figure 13(b), the first-break estimated average velocity is 8.34×10^7 m/s, and the peak estimate is 3.12×10^7 m/s. Given the relative permittivity of the slab is 15, the analytical calculation of average velocity is 7.75×10^7 m/s. This indicates an error of 59.7% in the peak estimation, while 7.7% is the error in the first-break estimation. The results obtained with Nahanni measurements indicate that the first-break determination using the MER algorithm is able to provide robust performance with either reflection or transmission data that exhibit a great deal of waveform distortion. On the contrary, the peak approach can be severely affected by the waveform modification and is incapable of providing a reliable solution without user selection of the appropriate part of the waveform.

The first-breaks shown in Figure 13 are the results of applying the mis-pick correction to the first-breaks determined by the MER algorithm. Figure 14 compares the least-squares best-fit lines constructed before and after the mis-pick correction. The two mis-picks at time zero are due to the non-zero samples injected by truncating the signal prior to the antenna aperture. They yield a best-fit line that corresponds to a negative wave travel velocity. The actual first-break should be picked from the sample location exhibiting the second largest ER value. After the correction, the first-breaks closely align with the best-fit line, which indicates a more accurate estimation of the wave travel velocity in the dielectric slab.

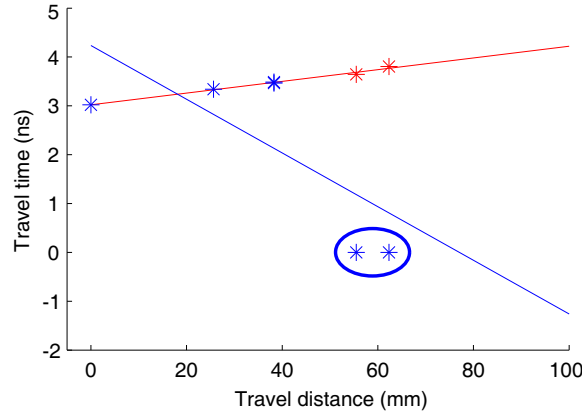


Figure 14. Demonstration of mis-pick correction. The blue ‘*’ represents the first-breaks before mis-pick correction and the blue line is the least-squares fit of these picks. The red line is the best-fit line after correcting the mis-picks circled in blue to the right positions indicated by the red ‘*’.

4.5. Impact of Antenna Aperture and Average Velocity on Images

For a microwave imaging system, the antenna aperture time serves as a reference that is used to correct the arrival time of reflected or transmitted waves from an object. Given the geometry of the imaging space, the velocity determines the wave travel time. The correct reference location and travel time calculation are essential for radar-based image reconstruction algorithms to yield an accurate representation of the imaged object. To investigate the impact of the antenna aperture and the corresponding average velocity in the immersion medium on the images, 2D images are constructed with the simulated sphere responses (Section 3.2) via the confocal imaging algorithm (Section 3.5). The results obtained from the first-break estimates and the peak estimates are demonstrated and compared.

Figure 15 shows the 2D images created for spheres with diameters of 2 mm and 20 mm. In a pair of images, the results of focusing using the first-break estimates of antenna aperture and velocity are shown first. Following each set of images is the alignment of responses recorded at the location of the maximum response in the image.

Based on the metrics defined in Section 3.6, Table 2 compares the images reconstructed with the first-break estimates and the peak estimates for the sphere with diameter of 2 mm. The first-break estimates give a better image than the peak estimates in terms of larger SMR value and narrower

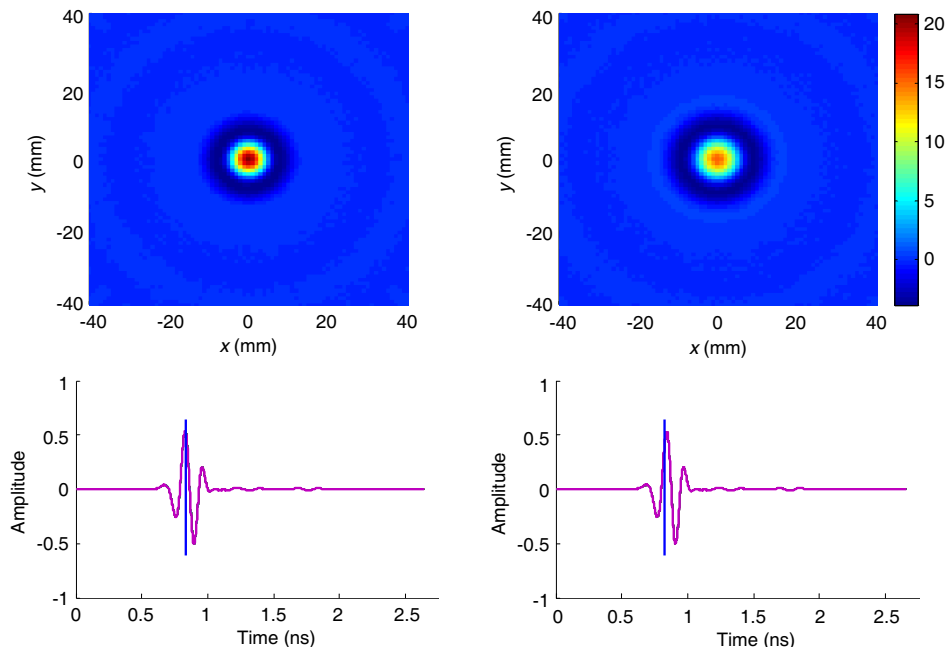
Table 2. Comparison of images of 2 mm diameter sphere reconstructed using different estimates of antenna aperture time and average velocity.

Metrics	First-break	Peak
SMR (dB)	27.38	25.08
FWHM (mm)	6.35	7.68
Location Error (mm)	0	0

FWHM. Both methods give correct estimation of the object location and the signals are closely aligned at the location of the maximum response in the image. While the alignment with the first break estimates is at the peak location in the signal, a slight shift from the peak location is observed with the peak estimates.

An interesting observation can be made that, with the peak estimates, the maximum response lies at the center for both 2 mm and 20 mm spheres. In other word, the maximum response does not correspond to the change in the object size. However, with the first-break estimates, the maximum response shifts from the center to the surface and forms a circle. In other word, this shift gives us a sense of the variation in the object size. This shift is also reflected in the alignment plots in Figure 15(b), which ultimately causes difference in the final images. Other than the 2 mm and 20 mm spheres, we reconstruct the images for the spheres with diameter between 4 mm and 18 mm. Together, the results indicate that, with the first-break estimates, when the sphere has a diameter greater than 16 mm, the maximum response shifts from the center to the surface; when the diameter is equal to or smaller than 16 mm, the maximum response stays in the center. On the other hand, with the peak estimates, the maximum response stays in the center and does not corresponds to the change in the sphere size.

Similar results are obtained from the spheres with loss. However, in this case, the reconstructed images do not exhibit as many ‘rings’ as those reconstructed with the lossless spheres, especially when the sphere diameter is greater than 8 mm. The ringing effect comes from the multiple paths and multiple reflections as the wave propagates through the sphere. When the sphere is lossy, the multiple paths and multiple reflections are reduced, resulting in fewer rings in the reconstructed images. Furthermore, we reconstruct the 3D image for the carbon-based tumor phantom. The tumor phantom is roughly spherical and has a diameter of 16 mm. With the scan pattern described in Figure 6, the antenna array



(a)

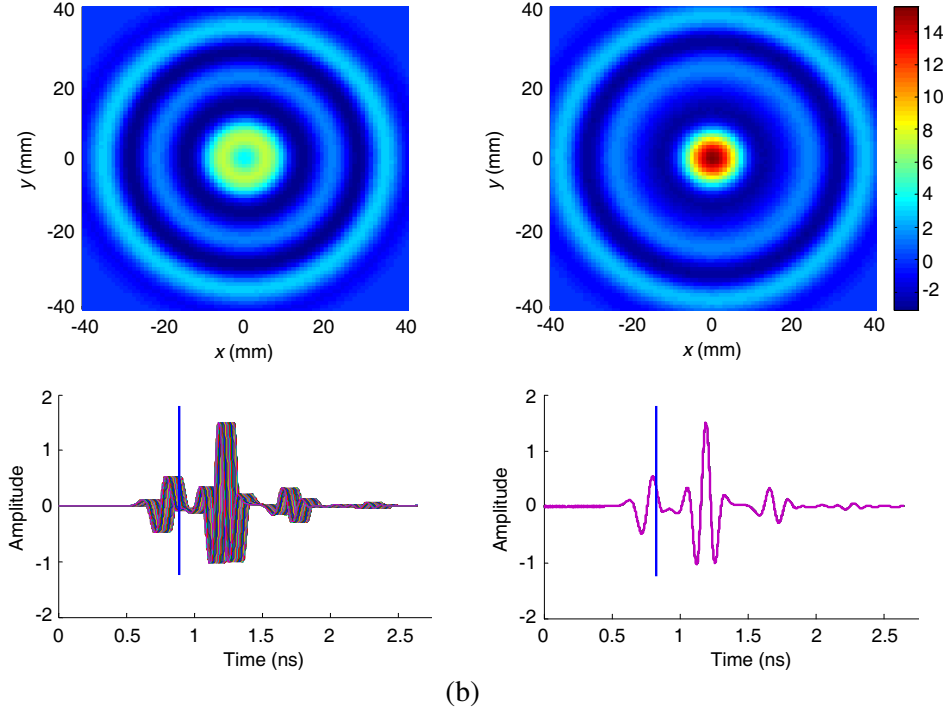


Figure 15. Time focusing and alignment responses at the location of the maximum response in the image. Sphere has diameter of (a) 2 mm and (b) 20 mm. The results from the first-break method are displayed on the left column, and those from the peak method are shown on the right column. The blue line in the alignment plots corresponds to the location of the maximum response in the image.

is not symmetric around the tumor phantom, i.e., the antenna array extends further in $-z$ direction. Therefore, instead of the calculated center at (20 mm, 0, -40 mm), the maximum response in the image corresponds to a location at (20 mm, 0, -47 mm) with the first-break estimates and a location at (20 mm, 0, -45 mm) with the peak estimates. In either case, similar energy spreading curves across the maximum response location are observed between the tumor phantom and the simulated spheres with a diameter of 16 mm.

Overall, because the canola oil is low loss and non-dispersive, the differences between the first-break estimates and the peak estimates are not large. Even with these small differences, the first-break images still provide more information regarding the size than those reconstructed using the peak estimates.

5. CONCLUSION

In this study, the concept of first-break in wave propagation has been introduced to microwave imaging for medical applications. In particular, we demonstrate the technique of using first-break as references to determine antenna aperture time for microwave breast imaging systems. The performance of the first-break method is examined by simulated and measured data that include waveform distortion due to nonstationarity in wave propagation, superposition of multiple wavelets, and variation of excitation pulses.

The results imply that the first-break method is able to process either the reflection data or the transmission data collected by antennas with different structures. Compared to those readily identifiable characteristics in the signal, i.e., the peak response, the first-break is less influenced by waveform distortion and is able to provide more consistent reference. In the presence of waveform modification, the first-break estimates of the antenna aperture and the average velocity are more consistent and reliable than those estimated by the peak response. The results also imply that, in the case of limited waveform modification, similar estimates are obtained from both methods. Even though the differences

in the estimated antenna aperture and average velocity are small, the images reconstructed by using the first-break estimates are more sensitive to the change in the object size than those reconstructed by using the peak estimates.

ACKNOWLEDGMENT

This work is financially supported by the Natural Sciences and Engineering Research Council of Canada (NSERC), the Alberta Innovates Technology Futures (AITF), NSERC Collaborative Research and Training Experience (CREATE) Program, and the University of Calgary. The authors are grateful to Dr. Joe Wong for sharing his idea in first-break time picking, and deeply appreciate his comments and suggestions. The authors thank Jeremie Bourqui for his help on antenna measurement systems. Finally, the authors wish to thank the Consortium for Research in Elastic Wave Exploration Seismology (CREWES) for providing the software support.

REFERENCES

1. Meaney, P. M., M. W. Fanning, T. Raynolds, C. J. Fox, Q. Q. Fang, C. A. Kogel, et al., "Initial clinical experience with microwave breast imaging in women with normal mammography," *Acad. Radiol.*, Vol. 14, No. 2, 207–218, Feb. 2007.
2. Klemm, M., J. A. Leendertz, D. Gibbins, I. J. Craddock, A. Preece, and R. Benjamin, "Microwave radar-based differential breast cancer imaging: Imaging in homogeneous breast phantoms and low contrast scenarios," *IEEE Trans. Antennas Propag. Mag.*, Vol. 58, No. 7, 2337–2344, Apr. 2010.
3. Persson, M., X. Zeng, and A. Fhager, "Microwave imaging for medical applications," *Proceedings of the 5th EUCAP*, 3070–3072, 2011.
4. Fear, E. C., J. Bourqui, C. Curtis, D. Mew, B. Docktor, and C. Romano, "Microwave breast imaging with a monostatic radar-based system: A study of application to patients," *IEEE Trans. Microw. Theory Techn.*, Vol. 61, No. 5, 2119–2128, May 2013.
5. Aguilar, S. M., M. A. Al-Joumayly, M. J. Burfeindt, N. Behdad, and S. C. Hagness, "Multiband miniaturized patch antennas for a compact, shielded microwave breast imaging array," *IEEE Trans. Antennas Propag. Mag.*, Vol. 62, No. 3, 1221–1231, Mar. 2014.
6. Nikolova, N. K., "Microwave imaging for breast cancer," *IEEE Microw. Mag.*, Vol. 12, No. 7, 78–94, Dec. 2011.
7. Allaby, M., *A Dictionary of Earth Sciences*, Oxford University Press, UK, 2008.
8. Yilmaz, O., *Seismic Data Analysis: Processing, Inversion, and Interpretation of Seismic Data*, Society of Exploration Geophysicists, Tulsa, OK, USA, 2001.
9. Sabbione, J. I. and D. Velis, "Automatic first-breaks picking: New strategies and algorithms," *Geophysics*, Vol. 75, No. 4, V67–V76, Jul.–Aug. 2010.
10. Wong, J., L. Han, J. C. Bancroft, and R. R. Stewart, "Automatic time-picking of first arrivals on noisy microseismic data," *CREWES Research Rep.*, Vol. 21, No. 30, Dec. 2009.
11. Molyneux, J. B. and D. R. Schmitt, "First-break timing: Arrival onset times by direct correlation," *Geophysics*, Vol. 64, No. 5, 1492–1501, Sep.–Oct. 1999.
12. Peraldi, R. and A. Clement, "Digital processing of refraction data study of first arrivals," *Geophys. Prospect.*, Vol. 20, No. 3, 529–548, Sep. 1972.
13. Coppens, F., "First arrival picking on common-offset trace collections for automatic estimation of static corrections," *Geophys. Prospect.*, Vol. 33, No. 8, 1212–1231, Dec. 1985.
14. Hatherly, P. J., "A computer method for determining seismic first arrival times," *Geophysics*, Vol. 47, No. 10, 1431–1436, Oct. 1982.
15. Han, L., "Microseismic monitoring and hypocenter location," M.S. Thesis, Dept. GeoSci., Univ. Calgary, Calgary, AB, Canada, 2010.
16. Bourqui, J., "Balanced antipodal Vivaldi antenna and dielectric director for breast cancer detection," M.S. Thesis, Dept. Elect. Eng., Univ. Calgary, Calgary, AB, Canada, 2008.

17. Taylor, J. R., *An Introduction to Error Analysis: The Study of Uncertainties in Physical Measurements*, University Science Books, Sausalito, CA, 1982.
18. Bourqui, J. and E. C. Fear, "Shielded UWB sensor for biomedical applications," *IEEE Antennas Wireless Propag. Lett.*, Vol. 11, 1614–1617, Dec. 2012.
19. Garrett, J. and E. Fear, "Stable and flexible materials to mimic the dielectric properties of human soft tissues," *IEEE Antennas Wireless Propag. Lett.*, Vol. 13, 599–602, Apr. 2014.
20. Bourqui, J. and E. C. Fear, "Biological tissues assessment using transmitted microwave signals," *Proceedings of the 8th EUCAP*, 77–78, 2014.
21. Ulriksson, B., "Conversion of frequency-domain data to the time domain," *Proc. IEEE*, Vol. 74, No. 1, 74–77, Jan. 1986.
22. *SEMCAD X Reference Guide*, Schmid & Partner Engineering AG, Zürich, Switzerland, 2012.
23. Ray, P. S., J. J. Stephens, and T. W. Kitterman, "Near-field impulse response examination of backscattering from dielectric spheres," *Appl. Opt.*, Vol. 14, No. 10, 2492–2498, Oct. 1975.